
Sketch Then Paint: Hierarchical Reinforcement Learning for Diffusion Multi-Modal Large Language Models

Siqu Luo^{1,2,*}, Jianghan Shen^{2,3,*}, Yi Xin^{3,4}, Huayu Zheng¹, Haoxing Chen³, Yan Tai¹, Qi Qin²,
Yue Li⁵, Junjun He^{2,4}, Yihao Liu², Guangtao Zhai¹, Yuewen Cao², Xiaohong Liu^{1,4,†}

¹Shanghai Jiao Tong University, ²Shanghai Artificial Intelligence Laboratory, ³Nanjing University,
⁴Shanghai Innovation Institute, ⁵Peking University

 Code: <https://github.com/Alpha-VLLM/Lumina-DiMOO>

Abstract

Diffusion Multi-Modal Large Language Models (dMLLMs) are powerful for image generation, but optimizing them through reinforcement learning (RL) remains a major challenge. One primary difficulty is that a single image can be generated through many different unmasking sequences, which makes calculating importance ratios is often intractable. Additionally, existing methods tend to ignore the hierarchical generation process of dMLLMs, where early tokens define the global layout and later tokens focus on local details. By assigning uniform rewards to all tokens, these current methods fail to reflect the actual contribution of each token to the final image. To address these issues, we propose **Hierarchical Token GRPO (HT-GRPO)**, which integrates this hierarchy directly into the policy optimization process. Our approach features a Sketch-Then-Paint training scheme that organizes updates into three distinct stages: global, structure, and refinement. We also use a prompt-conditioned estimator to calculate importance ratios starting from a fully masked state. Furthermore, we introduce a Hierarchical Credit Assignment mechanism that prioritizes key structural tokens to ensure accurate reward propagation. Experiments using two popular dMLLM backbones, MMaDA and Lumina-DiMOO, demonstrate that HT-GRPO achieves substantial gains on the GenEval and DPG benchmarks. Evaluations across six additional metrics confirm significant improvements in image quality, aesthetics, and human preference.

1 Introduction

Recent advancements in text-to-image (T2I) generation, driven by powerful diffusion models [1, 2, 3, 4] and autoregressive (AR) models [5, 6, 7, 8], have achieved significant breakthroughs. This success is largely built upon the scaling of computational resources, model parameters, and training data. Alongside these efforts, the integration of reinforcement learning (RL) [9, 10, 11, 12] has also become an essential component. By effectively aligning generation outputs with human preferences (e.g., prompt adherence, aesthetic), RL significantly improves the performance of T2I models. More recently, Diffusion Multi-Modal Large Language Models (dMLLMs) [13, 14, 15, 16, 17, 18] have emerged as a significant architectural evolution. By performing parallel iterative denoising over discrete tokens, dMLLMs offer a novel approach to visual generation. This architectural shift naturally requires researchers to design RL strategies specifically tailored for dMLLMs. The generation process of dMLLMs is inherently hierarchical: tokens decoded early shape global layout under high uncertainty, while tokens decoded late refine local details under low uncertainty.

*Equal contribution †Corresponding author: xiaohongliu@sjtu.edu.cn

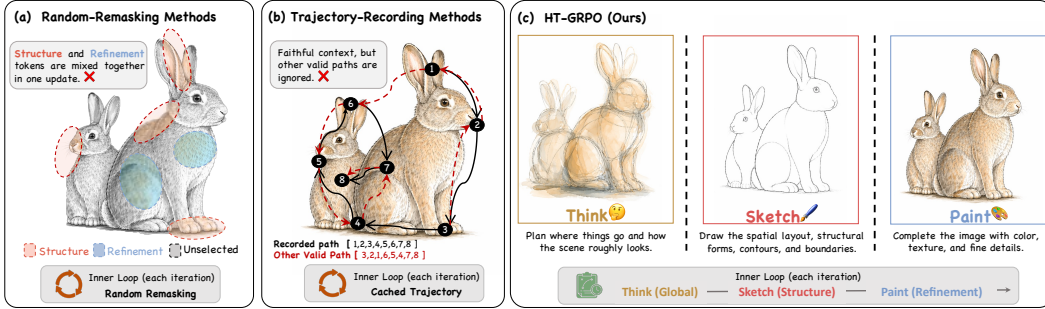


Figure 1: Comparison of RL inner-loop strategies for dMLLMs.

Existing RL approaches generally follow two routes, but both fail to account for this structure: **1) Random remasking methods** (shown in Figure 1(a)) [19, 20, 21] approximate intermediate states by randomly remasking tokens in generated images and evaluating selected tokens under the remaining visible context (*Limitation: future-token contamination*). However, this earliest naive paradigm leaks future information into the selected step. It also arbitrarily mixes structural tokens responsible for global layout with refinement tokens responsible for local details into the same gradient update, preventing the model from optimizing each group at its appropriate stage (*Limitation: stage conflation*). **2) Trajectory recording methods** (shown in Figure 1(b)) [22, 23, 24, 25] build a more explicit decision process by storing actual denoising trajectory. While this prevents information leakage, the inner-loop updates for each generated image are bound to a single recorded ordering, ignoring the many other valid unmasking orderings (*Limitation: narrow path coverage*). Beyond these specific issues, both routes assign uniform image-level rewards to all tokens, ignoring the fact that different tokens have entirely different impacts on the final image quality (*Shared Limitation: uniform token reward*).

To overcome these limitations, we propose Hierarchical Token GRPO (HT-GRPO), a novel RL method that explicitly encodes the hierarchical structure of dMLLM generation into inner-loop policy optimization. HT-GRPO consists of two core components. **First, we propose a Sketch-Then-Paint staged training framework.** This organizes the inner-loop updates into three consecutive stages (shown in Figure 1(c)): a Global stage that updates all tokens jointly to establish a stable coarse foundation, a Structure stage that focuses exclusively on structural tokens to sharpen global composition, and a Refinement stage that polishes local details only after the structure is settled, preventing structural and refinement tokens from being mixed in the same gradient update. Within each stage, random subset sampling covers multiple valid generation paths at the same semantic level. This enables the model to explore and optimize over a rich set of semantically consistent generation paths. To support this staged optimization, we further introduce a **prompt-conditioned estimator** that computes token-level importance ratios under a unified fully masked state using only the text prompt as condition. This simultaneously eliminates future-token contamination, prevents low-entropy degradation when evaluating refinement tokens, and removes the need to cache any intermediate denoising states. **Second, we introduce Hierarchical Credit Assignment.** This assigns higher credit weights to early structural tokens and lower weights to later refinement tokens, ensuring that image-level rewards are distributed in proportion to each token’s actual contribution.

Extensive experiments confirm that HT-GRPO delivers superior text-image alignment on multiple benchmarks. On the MMaDA model, it raises GenEval from 0.56 to 0.83 and DPG from 70.51 to 81.09. When applied to Lumina-DiMOO, these scores further improve to 0.92 and 84.47 respectively. Additionally, HT-GRPO significantly boosts performance across six metrics covering image quality, aesthetics, and human preference. These results confirm that hierarchical token optimization is a versatile and effective approach. Overall, our contributions can be summarized as follows:

- We reveal that the intrinsic hierarchical structure of dMLLM generation is essential. Existing RL methods ignore it, leading to stage conflation and inaccurate reward broadcasts. Instead, we explicitly leverage this structure to achieve principled hierarchical policy optimization.
- We propose **Sketch-Then-Paint** staged training, which divides inner-loop updates into Global, Structure, and Refinement stages by generation order, and uses a prompt-conditioned estimator to prevent future-token contamination without caching trajectories.
- We design **Hierarchical Credit Assignment** to allocate generation-order-aware weights to different tokens. This effectively aligns the reward propagation with the actual contribution of each token.

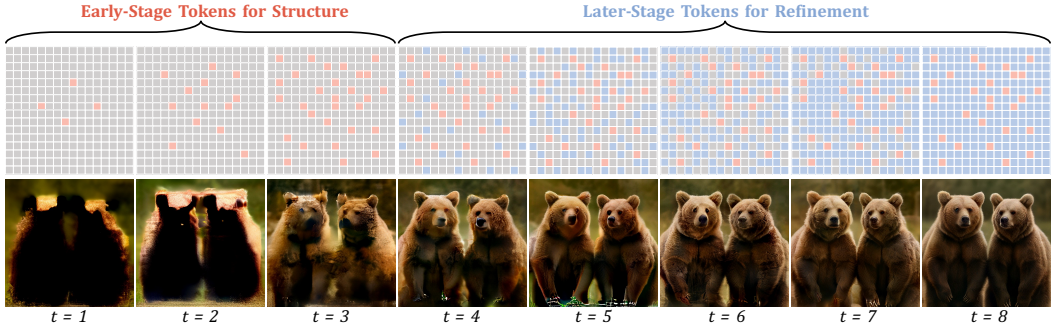


Figure 2: **Visualization of the image generation process in dMLLMs.** Top: early (red, structure) tokens set layout, later (blue, refinement) tokens add detail. Bottom: depict the corresponding outputs.

- We show that HT-GRPO consistently enhances MMaDA and Lumina-DiMOO across various benchmarks. This confirms the strong generalization of hierarchical token optimization across dMLLM architectures, outperforming leading T2I models.

2 Preliminaries

2.1 Image Generation Process of dMLLMs

dMLLMs generate images by iteratively denoising masked visual tokens. An image is represented as a token sequence of length N with text condition c . Starting from a fully masked state $\mathbf{x}^{(T)}$, the model repeatedly unmasks a subset of positions until the final image $\mathbf{x}^{(0)} = (v_1, \dots, v_N)$ is produced:

$$\mathbf{x}^{(t-1)} \sim \pi_{\theta}(\cdot | \mathbf{x}^{(t)}, c), \quad t = T, T-1, \dots, 1. \quad (1)$$

Unlike autoregressive models, which generate tokens in a fixed left-to-right order, dMLLMs can produce the same image through many different unmasking orderings. We track this ordering with the generation-order rank $\rho_{g,i} \in \{1, \dots, N\}$: rank 1 is the first position unmasked and rank N the last. Tokens unmasked in the same step receive consecutive ranks under an arbitrary fixed order within that step.

The rank $\rho_{g,i}$ reflects a fundamental asymmetry in what the model knows at prediction time. A token with small $\rho_{g,i}$ is unmasked early, when most of the image is still masked. It faces high uncertainty, and its choice largely determines where objects appear and how the scene is organized. A token with large $\rho_{g,i}$ is unmasked late, after most of the image has been revealed. It faces much lower uncertainty and mainly refines color, texture, and local detail. We call tokens with small $\rho_{g,i}$ *structural tokens* and tokens with large $\rho_{g,i}$ *refinement tokens* (Figure 2). [Proposition C.1](#) provides a formal characterization of this entropy gap. This rank-induced asymmetry becomes a key challenge when applying RL to dMLLMs, as formalized in Section 2.2.

2.2 Group Relative Policy Optimization

GRPO [26] maximizes a clipped surrogate objective over G rollouts sampled from a behavior policy $\pi_{\theta_{\text{old}}}$, using per-token importance ratios and group-relative advantages; the standard formulation is recalled in Appendix D.

Applying GRPO to dMLLMs. Extending the token-level GRPO objective to dMLLMs rests on two properties of Eq. (1). First, *Markov chain decomposition*: along a fixed unmasking trajectory, the joint probability factorizes step-wise via the chain rule. Second, *within-step conditional independence*: conditioned on the current state $\mathbf{x}^{(t)}$ and text prompt c , the tokens unmasked at step t are sampled independently across positions. Together, these two properties enable a per-token formulation of the importance ratio in dMLLMs, analogous to the autoregressive case (Appendix D).

Assumption 1 (Stage-varying optimization). *Because dMLLMs decode tokens across T stages under progressively changing visual contexts, the per-step optimization objective is inherently non-uniform. We therefore introduce an optimization support set $\mathcal{M}_g^{(k)}$ and a conditioning context $\mathbf{C}_{g,i}^{(k)}$*

to characterize each gradient step k . All methods discussed in this paper are special instantiations of this paradigm. A unified comparison is given in Appendix B.

Under Assumption 1, the objective at gradient step $k \in \{1, \dots, K\}$ is:

$$\mathcal{J}^{(k)}(\theta) = \mathbb{E}_{c, \{\mathbf{x}_g^{(0)}\} \sim \pi_{\theta_{\text{old}}}} \left[\frac{1}{G} \sum_{g=1}^G \frac{1}{|\mathcal{M}_g^{(k)}|} \sum_{i \in \mathcal{M}_g^{(k)}} \min \left(r_{g,i}^{(k)}(\theta) A_g, \text{clip} \left(r_{g,i}^{(k)}(\theta), 1-\epsilon, 1+\epsilon \right) A_g \right) - \beta \mathbb{D}_{\text{KL}}(\pi_{\theta} \parallel \pi_{\text{ref}}) \right], \quad (2)$$

where the per-token importance ratio

$$r_{g,i}^{(k)}(\theta) = \frac{\pi_{\theta}(v_{g,i} \mid \mathbf{C}_{g,i}^{(k)}, c)}{\pi_{\theta_{\text{old}}}(v_{g,i} \mid \mathbf{C}_{g,i}^{(k)}, c)} \quad (3)$$

measures the relative likelihood of visual token $v_{g,i}$ under the current versus behavior policy, conditioned on the visual context $\mathbf{C}_{g,i}^{(k)}$ and text context c . The group-relative advantage $A_g = (R_g - \text{mean}(\{R_j\})) / (\text{std}(\{R_j\}) + \delta)$ is a scalar broadcast uniformly to every token in rollout g .

Remark 1. Each rollout produces one image $\mathbf{x}_g^{(0)}$ via a single unmasking trajectory. The same image could have been generated through exponentially many alternative orderings, each inducing a different conditioning context $\mathbf{C}_{g,i}^{(k)}$ for every token. The ideal objective averages Eq. (2) over all valid trajectories:

$$\mathcal{J}^*(\theta) = \mathbb{E}_{\tau \sim \pi_{\theta_{\text{old}}}} [\mathcal{J}_{\tau}(\theta)], \quad (4)$$

where \mathcal{J}_{τ} denotes Eq. (2) instantiated with $\mathcal{M}_g^{(k)} = \{1, \dots, N\}$ and $\mathbf{C}_{g,i}^{(k)}$ set to the tokens unmasked before position i under trajectory τ . This expectation is intractable in practice.

2.3 Limitations of Existing Methods

As noted in Remark 1, \mathcal{J}^* is intractable in practice. Existing methods therefore approximate it by making different choices of $\mathcal{M}_g^{(k)}$ and $\mathbf{C}_{g,i}^{(k)}$. Random remasking methods construct diverse pseudo-trajectories through random masking, while trajectory recording methods condition on the single observed trajectory. Each approximation carries its own limitations, analyzed below. A unified formal comparison is provided in Appendix B.

Random Remasking Methods. MaskGRPO [19], D1 [20], and UniGRPO [21] schedule $\mathcal{M}_g^{(k)}$ by progressively increasing the mask ratio across the K gradient steps. At each step k , the conditioning context $\mathbf{C}_{g,i}^{(k)}$ consists of the randomly retained visible tokens together with the text prompt c . This construction introduces two limitations. First, *future-token contamination*: the randomly retained tokens are not ordered by generation rank. The context $\mathbf{C}_{g,i}^{(k)}$ may therefore include tokens not yet unmasked when position i was originally generated, making it causally inconsistent, as shown in Proposition C.2. Second, *stage conflation*: the progressive mask schedule assigns tokens to $\mathcal{M}_g^{(k)}$ without regard to generation-order rank $\rho_{g,i}$. Structural tokens and refinement tokens are thus mixed in the same gradient update despite their fundamentally different entropy levels, as established in Section 2.1 and formalized in Proposition C.1. On the other hand, the random remasking strategy provides multi-path coverage. By randomly varying the masked tokens across gradient steps, these methods expose the model to multiple partial views of the same generated image, providing broader context diversity than a single fixed trajectory.

Trajectory Recording Methods. TraceRL [22], CJ-GRPO [23], d-TreeRPO [24], and AGRPO [25] set $\mathcal{M}_g^{(k)}$ to all N token positions at every gradient step. The conditioning context $\mathbf{C}_{g,i}^{(k)}$ is the set of tokens already unmasked just before position i was revealed during the rollout trajectory. By grounding the context in the actual generation order, these methods avoid both future-token contamination and stage conflation. They introduce two limitations of their own, however. First, *limited path coverage*: as discussed in Remark 1, the ideal \mathcal{J}^* requires averaging over all valid

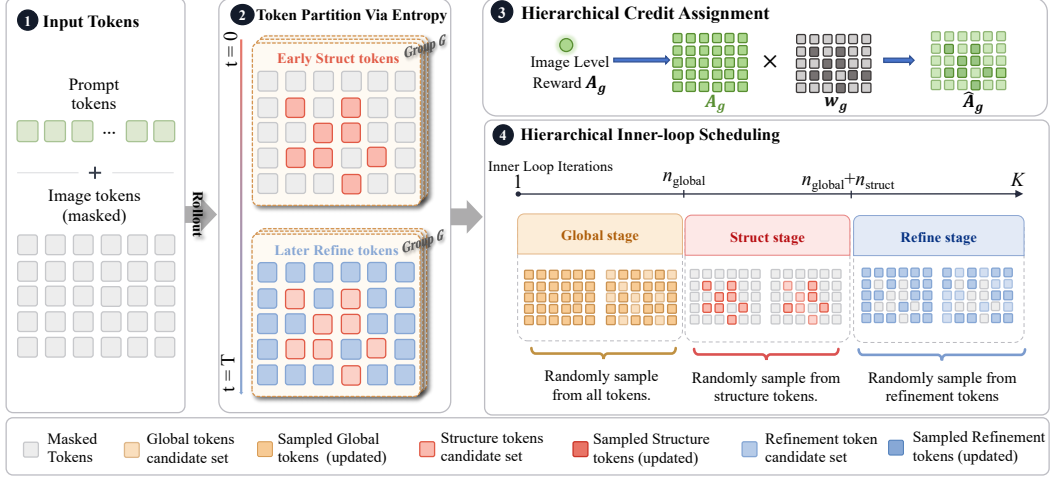


Figure 3: **HT-GRPO framework.** (1) Prompt and masked image tokens are rolled out to produce G sample groups. (2) Tokens are partitioned into structural (early, high-entropy) and refinement (later, low-entropy) sets via generation-order rank. (3) The image-level advantage A_g is reweighted by per-token credits $w_{g,i}$ to form the hierarchical advantage $\tilde{A}_{g,i}$. (4) Inner-loop updates are scheduled into three stages, each randomly sampling from its corresponding token set.

trajectories. Each rollout records only one ordering, so all alternatives remain unseen and the expectation is approximated by a single sample. Second, computational overhead: recording the full denoising trajectory requires storing all intermediate states and performing $O(T)$ forward passes per rollout. This substantially increases both memory usage and compute cost per training cycle.

Shared Limitation. Neither family accounts for the difference between structural and refinement tokens in the advantage assignment. The scalar A_g is broadcast uniformly to every token regardless of denoising stage, assigning equal credit to structural and refinement tokens despite their vastly different entropy levels.

3 Method

The limitations in Section 2.3 fall into two categories. The first concerns the approximation of \mathcal{J}^* : existing choices of $\mathcal{M}_g^{(k)}$ and $\mathbf{C}_{g,i}^{(k)}$ each introduce stage conflation, limited path coverage, or future-token contamination. The second concerns reward attribution: the image-level advantage A_g is broadcast uniformly, ignoring the entropy gap between structural and refinement tokens.

HT-GRPO addresses both categories through two components. Section 3.1 presents Sketch-Then-Paint staged training with a prompt-conditioned estimator. Inter-stage partitioning of $\mathcal{M}_g^{(k)}$ resolves stage conflation, intra-stage random subset sampling alleviates limited path coverage, and fixing $\mathbf{C}_{g,i}^{(k)} = \mathbf{C}_\emptyset$ eliminates future-token contamination. Section 3.2 replaces the uniform A_g with Hierarchical Credit Assignment.

3.1 Hierarchical Token GRPO

Visual generation is a progressive process from global structure to local detail, encoded in the distribution of $\rho_{g,i}$. As established in Section 2.1, tokens with small $\rho_{g,i}$ are structural tokens facing high uncertainty, while those with large $\rho_{g,i}$ are refinement tokens operating under rich context. HT-GRPO encodes this ordering into both the optimization schedule and the importance ratio estimator.

3.1.1 Sketch-Then-Paint Staged Training

Under standard GRPO, one policy optimization cycle is:

$$\pi_{\theta_{\text{old}}} \xrightarrow{\text{rollout}} \{\mathbf{x}_g^{(0)}\}_{g=1}^G \xrightarrow{\text{optimize}} \theta \xrightarrow{\text{synchronize}} \theta_{\text{old}} \leftarrow \theta. \quad (5)$$

The policy performs K inner-loop gradient updates on the same rollout batch. Although some methods vary which tokens enter each update, none account for the entropy-level distinction between structural and refinement tokens.

We organize the K inner-loop updates into three consecutive stages:

$$\text{Global} \rightarrow \text{Structure} \rightarrow \text{Refinement}. \quad (6)$$

This creates a coarse-to-fine curriculum from high entropy to low entropy. The Global stage first optimizes all tokens jointly to provide a stable starting point. The Structure stage then focuses on high-entropy tokens, and the Refinement stage finally optimizes low-entropy detail after the skeleton has been established. This progression reduces gradient interference between token groups with fundamentally different entropy regimes.

Let $N_s = \lfloor \alpha N \rfloor$ with $\alpha \in (0, 1)$ denoting the structure fraction. We define the stage-specific token sets as

$$\mathcal{S}_{g,\text{global}} = \{1, \dots, N\}, \mathcal{S}_{g,\text{structure}} = \{i \mid \rho_{g,i} \leq N_s\}, \mathcal{S}_{g,\text{refinement}} = \{i \mid \rho_{g,i} > N_s\}. \quad (7)$$

Here N_s is a token-count cutoff rather than a denoising-step cutoff. $\mathcal{S}_{g,\text{structure}}$ collects the N_s structural tokens with the smallest $\rho_{g,i}$ values, and $\mathcal{S}_{g,\text{refinement}}$ the remaining $N - N_s$ refinement tokens, following the taxonomy in Section 2.1. This partition depends only on the rollout’s own unmasking order and requires no external annotation. Using unmasking rank as an entropy proxy is justified by [Proposition C.1](#).

We split the total inner-loop budget as $K = n_{\text{global}} + n_{\text{structure}} + n_{\text{refinement}}$. For the k_s -th update inside stage s , where $k_s = 0, \dots, n_s - 1$, we independently sample a random subset $\mathcal{M}_g^{(k_s)} \subseteq \mathcal{S}_{g,s}$ according to an annealed sampling rate $\gamma_{k_s}^{(s)}$. Only tokens in $\mathcal{M}_g^{(k_s)}$ contribute gradients in that update:

$$\gamma_{k_s}^{(s)} = \gamma_{\min}^{(s)} + (\gamma_{\max}^{(s)} - \gamma_{\min}^{(s)}) \frac{\max(1, n_s - 1) - k_s}{\max(1, n_s - 1)}. \quad (8)$$

The sampling rate decays linearly from $\gamma_{\max}^{(s)}$ to $\gamma_{\min}^{(s)}$. Early updates cover more tokens and provide stable gradient directions, while later updates reduce computation and sharpen focus. Sampling different subsets $\mathcal{M}_g^{(k_s)}$ across inner-loop updates ensures that distinct portions of the token space receive gradient signal, rather than committing to a fixed subset throughout optimization. This intra-stage sampling acts as a Monte Carlo estimator over the token space within each stage, partially alleviating the limited path coverage identified in Section 2.3.

3.1.2 Prompt-Conditioned Estimator

Random remasking methods set $\mathbf{C}_{g,i}^{(k)}$ to a randomly retained subset of the generated image, which may expose tokens not yet visible at generation time and causes future-token contamination, as shown in [Proposition C.2](#). Trajectory recording methods avoid contamination by using the actual trajectory state, but require storing all intermediate denoising states and performing $O(T)$ forward passes per rollout cycle.

We instead use the fully masked initial state $\mathbf{x}^{(T)}$ as a unified conditioning context, denoted \mathbf{C}_\emptyset to emphasize that all N positions are masked, and define the prompt-conditioned importance ratio as

$$r_{g,i}(\theta) = \frac{\pi_\theta(v_{g,i} \mid \mathbf{C}_\emptyset, c)}{\pi_{\theta_{\text{oid}}}(v_{g,i} \mid \mathbf{C}_\emptyset, c)}. \quad (9)$$

Under a fully masked input, dMLLMs predict all N token distributions in a single forward pass, so all probabilities are obtained without caching any intermediate states. Using \mathbf{C}_\emptyset eliminates future-token contamination by construction, preserves predictive entropy for refinement tokens as shown in [Proposition C.3](#), and avoids the memory cost of trajectory recording.

3.2 Hierarchical Credit Assignment

Both families of existing methods uniformly broadcast the image-level advantage A_g to all tokens, assigning equal credit to structural and refinement tokens despite their fundamentally different roles.

Table 1: **Performance comparison on GenEval** across various dMLLMs and RL settings.

Methods	Single ↑	Two ↑	Counting ↑	Colors ↑	Position ↑	Attribute ↑	Overall ↑
<i>Text-to-Image Models</i>							
SDXL [27]	0.98	0.74	0.39	0.85	0.15	0.23	0.55
DALL-E 3 [28]	0.96	0.87	0.47	0.83	0.43	0.45	0.67
Janus-Pro [29]	0.99	0.89	0.59	0.90	0.79	0.66	0.80
FLUX.1-dev [30]	0.98	0.93	0.75	0.93	0.68	0.65	0.82
<i>dMLLMs (wo / w RL)</i>							
MMaDA [13]	0.96	0.60	0.45	0.81	0.14	0.25	0.56
+ UniGRPO [13]	0.99	0.76	0.61	0.84	0.20	0.37	0.63
+ MaskGRPO [19]	0.99	0.85	0.66	0.89	0.73	0.69	0.80
+ TraceGRPO [22]	1.00	0.87	0.72	0.92	0.64	0.62	0.79
+ HT-GRPO (Ours)	1.00	0.92	0.77	0.90	0.73	0.66	0.83
Lumina-DiMOO [14]	0.99	0.94	0.70	0.85	0.81	0.71	0.83
+ MaskGRPO [19]	1.00	0.90	0.88	0.89	0.85	0.77	0.88
+ TraceGRPO [22]	1.00	0.90	0.85	0.90	0.88	0.73	0.87
+ HT-GRPO (Ours)	1.00	0.95	0.94	0.93	0.93	0.75	0.92

We instead assign token-level credit weights according to generation order:

$$\tilde{A}_{g,i} = A_g \cdot w_{g,i}, \quad w_{g,i} = \begin{cases} \lambda_s, & i \in \mathcal{S}_{g,\text{structure}}, \\ \lambda_r, & i \in \mathcal{S}_{g,\text{refinement}}, \end{cases} \quad (10)$$

where $\lambda_s > 1 > \lambda_r \geq 0$. Structural tokens receive weights above the uniform baseline to amplify updates on global composition and layout, while refinement tokens receive smaller weights to attenuate updates on local detail. All three training stages share the same weighting scheme. The only difference across stages is which active token set $\mathcal{S}_{g,s}$ is selected.

The HT-GRPO per-step objective is Eq. (2) with A_g replaced by $\tilde{A}_{g,i}$:

$$\mathcal{J}^{(k)}(\theta) = \mathbb{E}_{c, \{\mathbf{x}_g^{(0)}\} \sim \pi_{\theta_{\text{old}}}} \left[\frac{1}{G} \sum_{g=1}^G \frac{1}{|\mathcal{M}_g^{(k)}|} \sum_{i \in \mathcal{M}_g^{(k)}} \min \left(r_{g,i}(\theta) \tilde{A}_{g,i}, \text{clip}(r_{g,i}(\theta), 1-\epsilon, 1+\epsilon) \tilde{A}_{g,i} \right) - \beta \mathbb{D}_{\text{KL}}(\pi_{\theta} \parallel \pi_{\text{ref}}) \right], \quad (11)$$

where the K updates are ordered as Global \rightarrow Structure \rightarrow Refinement, consistent with Appendix B.

4 Experiments

4.1 Experimental Setup

Models. We validate our proposed HT-GRPO on two popular open-source pre-trained dMLLMs: MMaDA [13] and Lumina-DiMOO [14]. Since other notable dMLLMs, such as LaViDa-O [17], are not open-source, we cannot include them in our experiments. Additionally, models like LLaDA-o [18] are not strictly dMLLMs because they rely on continuous diffusion for image generation, making them unsuitable as a base model.

Baselines. Our primary baselines include specialized T2I models (e.g., SDXL [27], FLUX.1-dev [30], DALL-E 3 [28], Janus-Pro [29]), as well as the base versions of MMaDA and Lumina-DiMOO. Furthermore, we compare various RL training strategies. Specifically, we evaluate MaskGRPO [19] on the same dMLLM backbones to highlight the advantages of HT-GRPO. We additionally compare against TraceGRPO, a trajectory-aware baseline that constructs causally consistent contexts from the recorded unmasking order. Following the implementation of TraceRL [22], we refer to this method as TraceGRPO. We also test UniGRPO to establish the performance bound for single-stage RL.

Benchmarks & Metrics. To evaluate T2I generation performance, we employ two related benchmarks: GenEval [31] and DPG-Bench [32]. GenEval, consisting of 553 text prompts, is the most

Table 2: **Performance comparison on DPG-Bench** across various dMLLMs and RL settings.

Model	Global \uparrow	Entity \uparrow	Attribute \uparrow	Relation \uparrow	Other \uparrow	Overall \uparrow
<i>Text-to-Image Models</i>						
SDXL [27]	83.27	82.43	80.91	86.76	80.41	74.65
DALL-E 3 [28]	90.97	89.61	88.39	90.58	89.83	83.50
Janus-Pro [29]	86.90	88.90	89.40	89.32	89.48	84.19
FLUX.1-dev [30]	74.35	90.00	88.96	90.87	88.33	83.84
<i>dMLLMs (wo / w RL)</i>						
MMaDA [13]	77.52	77.52	77.67	81.56	63.13	70.51
+ MaskGRPO [19]	80.92	79.52	85.41	83.05	69.12	75.81
+ TraceGRPO [22]	82.34	78.92	81.29	82.08	70.21	74.37
+ HT-GRPO (Ours)	89.76	87.62	86.58	88.86	81.83	81.09
Lumina-DiMOO [14]	81.17	89.96	88.10	89.64	79.95	81.86
+ MaskGRPO [19]	82.65	89.50	88.33	88.60	88.24	82.24
+ TraceGRPO [22]	84.89	89.65	88.23	90.24	84.28	82.62
+ HT-GRPO (Ours)	88.04	91.22	88.98	92.56	83.05	84.47

Table 3: **Human preference, image quality, and aesthetics comparison on DPG-Bench** across various dMLLMs and RL settings.

Methods	DeQA \uparrow	ImgReward \uparrow	HPSv3 \uparrow	UniPercept		
				Aesthetics \uparrow	Quality \uparrow	Structure \uparrow
MMaDA [13]	3.91	0.64	8.81	58.83	65.29	47.46
+ MaskGRPO [19]	4.05	0.83	9.40	59.02	67.07	48.15
+ TraceGRPO [22]	4.08	0.84	9.56	58.78	66.87	49.04
+ HT-GRPO (Ours)	4.07	0.86	10.46	59.29	67.91	49.45
Lumina-DiMOO [14]	4.03	0.84	11.60	56.66	66.27	43.12
+ MaskGRPO [19]	4.08	0.90	12.00	56.77	66.13	43.55
+ TraceGRPO [22]	4.10	0.88	11.28	57.68	67.21	43.89
+ HT-GRPO (Ours)	4.12	0.97	12.46	58.39	67.97	44.97

widely used benchmark to assess object-centric generation. In contrast, DPG-Bench includes 1,065 dense and complex prompts to evaluate how well the generated images align with the text. Beyond benchmark performance, we also measure the human preference, visual quality, and aesthetics of the generated images using ImageReward [33], DeQA [34], HPSv3 [35], and UniPercept [36].

Implementation Details. HT-GRPO is implemented on top of the MaskGRPO [19] codebase, inheriting its optimizer, reward, and RL loop. Specifically, we generate $G = 9$ rollouts per prompt. The final reward score is a combination of HPSv3 [35], CLIP score [37], and UniReward [38], maintaining the original KL penalty coefficient and fixing the classifier-free guidance at 3.5. HT-GRPO-specific settings are: structure ratio $\alpha = 0.3$, three-stage budget $n_{\text{global}} : n_{\text{structure}} : n_{\text{refinement}} = 2 : 4 : 2$ ($K = 8$), token-level credit weights $\lambda_s = 1.5$ and $\lambda_r = 0.5$, and linear-decay annealing ($\gamma_{\text{max}} = 1.0$, $\gamma_{\text{min}} = 0.5$, down mode). All experiments run on $8 \times$ A100-80G GPUs. More details in Appendix F.

4.2 Main Results

GenEval. As shown in Table 1, the evaluation on the GenEval benchmark highlights the advantages of HT-GRPO in three main aspects. First, HT-GRPO is highly effective and outperforms previous RL methods. For the MMaDA, our method increases the base overall score from 0.56 to 0.83, clearly outperforming UniGRPO (0.63), MaskGRPO (0.80), and TraceGRPO (0.79). Second, this performance gain is consistent across different dMLLMs. When applied to the stronger Lumina-DiMOO, HT-GRPO improves the overall score from 0.83 to 0.92 and outperforms MaskGRPO (0.88) and TraceGRPO (0.87). This proves that our method generalizes well to different dMLLMs. Finally,

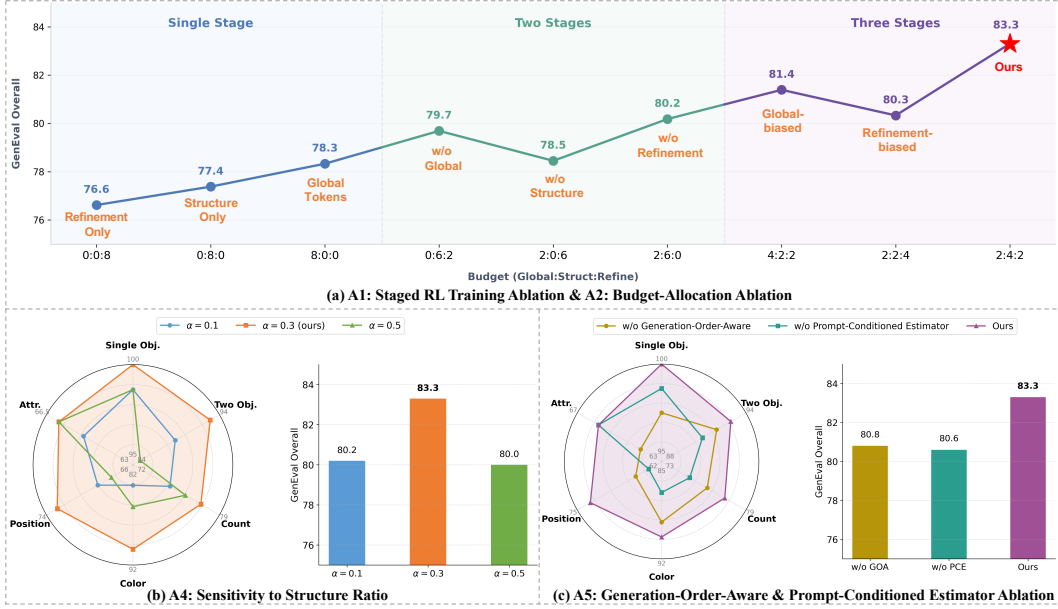


Figure 4: **(a) Stage organization and budget allocation:** The full Global→Structure→Refinement schedule with a structure-biased 2:4:2 budget consistently outperforms single-stage and two-stage variants. **(b) Sensitivity to structure ratio α :** Performance peaks at $\alpha = 0.3$ and degrades when the boundary is too narrow or too broad. **(c) Component analysis:** Hierarchical Credit Assignment and Prompt-Conditioned Estimator each provide independent gains, validating both design choices.

models trained with HT-GRPO are fully comparable to state-of-the-art T2I models. Leading models like FLUX.1-dev achieve an overall score of 0.82. MMDA with HT-GRPO reaches 0.83 to slightly pass them, and Lumina-DiMOO with HT-GRPO sets a new high score of 0.92.

DPG-Bench. DPG-Bench is more challenging than GenEval as it evaluates models using dense and complex prompts. As shown in Table 2, both MaskGRPO and TraceGRPO yield only marginal improvements over the Lumina-DiMOO baseline (82.24 and 82.62), with TraceGRPO even underperforming MaskGRPO on MMDA (74.37 vs. 75.81). In contrast, HT-GRPO successfully overcomes this performance bottleneck, raising the score to 84.47. This result surpasses leading models such as DALL-E 3 (83.50) and FLUX.1-dev (83.84), with similar gains observed when using the MMDA base model. Furthermore, Table 3 highlights another key advantage: HT-GRPO improves semantic alignment without sacrificing visual quality. It consistently achieves almost the highest scores across human preference metrics (e.g., ImageReward, HPSv3) and image quality & aesthetic evaluations (e.g., DeQA, UniPercept), proving that HT-GRPO effectively balances complex instruction following with high-fidelity image generation.

4.3 Ablation Study

Figure 4 and Table 5 (shown in Appendix E) summarize five ablation studies on MMDA ($K = 8$, $\alpha = 0.3$). **(a) Stage organization and budget:** The full Global→Structure→Refinement schedule with a 2:4:2 budget reaches 83.3 overall, outperforming all single-stage and two-stage variants (78.3–80.2); the coarse-to-fine ordering itself is critical. **(b) Structure ratio:** Performance peaks at $\alpha = 0.3$ and degrades for narrower ($\alpha = 0.1$, 80.2) and broader ($\alpha = 0.5$) boundaries, confirming that a well-calibrated hierarchy is essential. **(c) Component analysis:** Removing hierarchical credit weighting ($\lambda_s = \lambda_r = 1$) drops the score to 80.8, and replacing C_θ with revealed structural contexts reduces it to 80.6, validating both designs independently. The linear-decay annealing schedule (Table 5, 83.31) outperforms static and ascending baselines, confirming the value of broad initial coverage for stable gradient directions. Full per-ablation details are provided in Appendix E.

5 Conclusion

We revisit the application of GRPO to dMLLMs and identify two key challenges: multiple valid unmasking orderings make importance-ratio estimation difficult, while existing methods uniformly assign image-level rewards to tokens with heterogeneous roles. To address these issues, we propose HT-GRPO, which uses generation-order rank to characterize token uncertainty and role, organizes inner-loop updates into Global, Structure, and Refinement stages, estimates importance ratios under a fully masked prompt-conditioned context, and performs generation-order-aware credit assignment. Experiments on MMaDA and Lumina-DiMOO show consistent improvements across GenEval, DPG-Bench, and six human preference and visual quality metrics, demonstrating the effectiveness of hierarchical token optimization. A current limitation is that HT-GRPO uses a fixed structure ratio and fixed credit weights, which may not optimally adapt to prompts with different compositional complexity or rollout uncertainty. In the future, we will advance HT-GRPO through the integration of adaptive token grouping and dynamic credit assignment.

References

- [1] Huanqia Cai, Sihan Cao, Ruoyi Du, Peng Gao, Steven Hoi, Zhaohui Hou, Shijie Huang, Dengyang Jiang, Xin Jin, Liangchen Li, et al. Z-image: An efficient image generation foundation model with single-stream diffusion transformer. *arXiv preprint arXiv:2511.22699*, 2025.
- [2] Qi Qin, Le Zhuo, Yi Xin, Ruoyi Du, Zhen Li, Bin Fu, Yiting Lu, Jiakang Yuan, Xinyue Li, Dongyang Liu, et al. Lumina-image 2.0: A unified and efficient image generative framework. *Proceedings of the IEEE International Conference on Computer Vision (ICCV)*, 2025.
- [3] Chenfei Wu, Jiahao Li, Jingren Zhou, Junyang Lin, Kaiyuan Gao, Kun Yan, Sheng-ming Yin, Shuai Bai, Xiao Xu, Yilei Chen, et al. Qwen-image technical report. *arXiv preprint arXiv:2508.02324*, 2025.
- [4] Meituan LongCat Team, Hanghang Ma, Haoxian Tan, Jiale Huang, Junqiang Wu, Jun-Yan He, Lishuai Gao, Songlin Xiao, Xiaoming Wei, Xiaoqi Ma, et al. Longcat-image technical report. *arXiv preprint arXiv:2512.07584*, 2025.
- [5] Xinlong Wang, Xiaosong Zhang, Zhengxiong Luo, Quan Sun, Yufeng Cui, Jinsheng Wang, Fan Zhang, Yuezhe Wang, Zhen Li, Qiyang Yu, et al. Emu3: Next-token prediction is all you need. *arXiv preprint arXiv:2409.18869*, 2024.
- [6] Yufeng Cui, Honghao Chen, Haoge Deng, Xu Huang, Xinghang Li, Jirong Liu, Yang Liu, Zhuoyan Luo, et al. Emu3.5: Native multimodal models are world learners. *arXiv preprint arXiv:2510.26583*, 2025.
- [7] Yi Xin, Juncheng Yan, Qi Qin, Zhen Li, Dongyang Liu, Shicheng Li, Victor Shea-Jay Huang, Yupeng Zhou, Renrui Zhang, Le Zhuo, et al. Lumina-mgpt 2.0: Stand-alone autoregressive image modeling. *arXiv preprint arXiv:2507.17801*, 2025.
- [8] Dongyang Liu, Yi Xin, Shitian Zhao, Le Zhuo, Weifeng Lin, Xinyue Li, Qi Qin, Guangtao Zhai, Xiaohong Liu, Hongsheng Li, et al. Lumina-mgpt: Flexible photorealistic autoregressive text-to-image generation. *International Journal of Computer Vision (IJCV)*, 2026.
- [9] Jie Liu, Gongye Liu, Jiajun Liang, Yangguang Li, Jiaheng Liu, Xintao Wang, Pengfei Wan, Di Zhang, and Wanli Ouyang. Flow-grpo: Training flow matching models via online rl. *arXiv preprint arXiv:2505.05470*, 2025.
- [10] Zeyue Xue, Jie Wu, Yu Gao, Fangyuan Kong, Lingting Zhu, Mengzhao Chen, Zhiheng Liu, Wei Liu, Qiushan Guo, Weilin Huang, et al. Dancegrpo: Unleashing grpo on visual generation. *arXiv preprint arXiv:2505.07818*, 2025.
- [11] Zigang Geng, Yibing Wang, Yeyao Ma, Chen Li, Yongming Rao, Shuyang Gu, Zhao Zhong, Qinglin Lu, Han Hu, Xiaosong Zhang, et al. X-omni: Reinforcement learning makes discrete autoregressive image generative models great again. *arXiv preprint arXiv:2507.22058*, 2025.
- [12] Shihao Yuan, Yahui Liu, Yang Yue, Jingyuan Zhang, Wangmeng Zuo, Qi Wang, Fuzheng Zhang, and Guorui Zhou. Ar-grpo: Training autoregressive image generation models via reinforcement learning. *arXiv preprint arXiv:2508.06924*, 2025.
- [13] Ling Yang, Ye Tian, Bowen Li, Xinchen Zhang, Ke Shen, Yunhai Tong, and Mengdi Wang. MMaDA: Multimodal large diffusion language models. In *Advances in Neural Information Processing Systems*, volume 38, 2025.
- [14] Yi Xin, Qi Qin, Siqi Luo, Kaiwen Zhu, Juncheng Yan, Yan Tai, Jiayi Lei, Yuwen Cao, Keqi Wang, Yibin Wang, et al. Lumina-dimoo: An omni diffusion large language model for multi-modal generation and understanding. *arXiv preprint arXiv:2510.06308*, 2025.
- [15] Qingyu Shi, Jinbin Bai, Zhuoran Zhao, Wenhao Chai, Kaidong Yu, Jianzong Wu, Shuangyong Song, Yunhai Tong, Xiangtai Li, Xuelong Li, and Shuicheng Yan. Muddit: Liberating generation beyond text-to-image with a unified discrete diffusion model. In *International Conference on Learning Representations*, 2026.

- [16] Tiwei Bie, Haoxing Chen, Tiejuan Chen, Zhenglin Cheng, Long Cui, Kai Gan, Zhicheng Huang, Zhenzhong Lan, Haoquan Li, Jianguo Li, Tao Lin, Qi Qin, Hongjun Wang, Xiaomei Wang, Haoyuan Wu, Yi Xin, and Junbo Zhao. Llada2.0-uni: Unifying multimodal understanding and generation with diffusion large language model. *arXiv preprint arXiv:2604.20796*, 2026.
- [17] Shufan Li, Jiuxiang Gu, Kangning Liu, Zhe Lin, Zijun Wei, Aditya Grover, and Jason Kuen. Llada-o: Elastic large masked diffusion models for unified multimodal understanding and generation. *arXiv preprint arXiv:2509.19244*, 2025.
- [18] Zebin You, Xiaolu Zhang, Jun Zhou, Chongxuan Li, and Ji-Rong Wen. Llada-o: An effective and length-adaptive omni diffusion model. *arXiv preprint arXiv:2603.01068*, 2026.
- [19] Tianren Ma, Mu Zhang, Yibing Wang, and Qixiang Ye. Consolidating reinforcement learning for multimodal discrete diffusion models. *arXiv preprint arXiv:2510.02880*, 2025.
- [20] Siyan Zhao, Devaansh Gupta, Qinqing Zheng, and Aditya Grover. d1: Scaling reasoning in diffusion large language models via reinforcement learning. *arXiv preprint arXiv:2504.12216*, 2025.
- [21] Jie Liu, Zilyu Ye, Linxiao Yuan, Shenhan Zhu, Yu Gao, Jie Wu, Kunchang Li, Xionghui Wang, Xiaonan Nie, Weilin Huang, and Wanli Ouyang. UniGRPO: Unified policy optimization for reasoning-driven visual generation. *arXiv preprint arXiv:2603.23500*, 2026.
- [22] Yinjie Wang, Ling Yang, Bowen Li, Ye Tian, Ke Shen, and Mengdi Wang. Revolutionizing reinforcement learning framework for diffusion large language models. *arXiv preprint arXiv:2509.06949*, 2025.
- [23] Jingyi Yang, Guanxu Chen, Xuhao Hu, and Jing Shao. Taming masked diffusion language models via consistency trajectory reinforcement learning with fewer decoding step. *arXiv preprint arXiv:2509.23924*, 2025.
- [24] Leyi Pan, Shuchang Tao, Yunpeng Zhai, Zheyu Fu, Liancheng Fang, Minghua He, Lingzhe Zhang, Zhaoyang Liu, Bolin Ding, Aiwei Liu, and Lijie Wen. d-treerpo: Towards more reliable policy optimization for diffusion language models. *arXiv preprint arXiv:2512.09675*, 2025.
- [25] Anthony Zhan. Simple policy gradients for reasoning with diffusion language models. *arXiv preprint arXiv:2510.04019*, 2025.
- [26] Zhihong Shao, Peiyi Wang, Qihao Zhu, Runxin Xu, Junxiao Song, Xiao Bi, Haowei Zhang, Mingchuan Zhang, Y.K. Li, Y. Wu, and Daya Guo. Deepseekmath: Pushing the limits of mathematical reasoning in open language models. *arXiv preprint arXiv:2402.03300*, 2024.
- [27] Dustin Podell, Zion English, Kyle Lacey, Andreas Blattmann, Tim Dockhorn, Jonas Müller, Joe Penna, and Robin Rombach. Sdxl: Improving latent diffusion models for high-resolution image synthesis. *arXiv preprint arXiv:2307.01952*, 2023.
- [28] James Betker, Gabriel Goh, Li Jing, Tim Brooks, Jianfeng Wang, Linjie Li, Long Ouyang, Juntang Zhuang, Joyce Lee, Yufei Tian, et al. Improving image generation with better captions. *Technical Report, OpenAI*, 2023.
- [29] Xiaokang Chen, Zhiyu Wu, Xingchao Liu, Zizheng Pan, Wen Liu, Zhenda Xie, Xingkai Yu, and Chong Ruan. Janus-pro: Unified multimodal understanding and generation with data and model scaling. *arXiv preprint arXiv:2501.17811*, 2025.
- [30] Black Forest Labs. FLUX.1, 2024. Official model release.
- [31] Dhruva Ghosh, Hannaneh Hajishirzi, and Ludwig Schmidt. Geneval: An object-focused framework for evaluating text-to-image alignment. In *Advances in Neural Information Processing Systems*, volume 36, pages 76341–76366, 2023.
- [32] Xiwei Hu, Rui Wang, Yixiao Fang, Bin Fu, Pei Cheng, and Gang Yu. ELLA: Equip diffusion models with llm for enhanced semantic alignment. *arXiv preprint arXiv:2403.05135*, 2024. Introduces DPG-Bench.

- [33] Jiazheng Xu, Xiao Liu, Yuchen Wu, Yuxuan Tong, Qinkai Li, Ming Ding, Jie Tang, and Yuxiao Dong. Imagereward: learning and evaluating human preferences for text-to-image generation. In *Advances in Neural Information Processing Systems (NeurIPS)*, 2023.
- [34] Zhiyuan You, Xin Cai, Jinjin Gu, Tianfan Xue, and Chao Dong. Teaching large language models to regress accurate image quality scores using score distribution. In *Proceedings of the IEEE Conference on Computer Vision and Pattern Recognition (CVPR)*, 2025.
- [35] Yuhang Ma, Xiaoshi Wu, Keqiang Sun, and Hongsheng Li. Hpsv3: Towards wide-spectrum human preference score. *arXiv preprint arXiv:2508.03789*, 2025.
- [36] Shuo Cao, Jiayang Li, Xiaohui Li, Yuandong Pu, Kaiwen Zhu, Yuanting Gao, Siqi Luo, Yi Xin, Qi Qin, Yu Zhou, Xiangyu Chen, Wenlong Zhang, Bin Fu, Yu Qiao, and Yihao Liu. Unipercept: Towards unified perceptual-level image understanding across aesthetics, quality, structure, and texture. *arXiv preprint arXiv:2512.21675*, 2025.
- [37] SUN Zhengwentai. clip-score: CLIP Score for PyTorch. <https://github.com/taited/clip-score>, March 2023. Version 0.2.1.
- [38] Yibin Wang, Yuhang Zang, Hao Li, Cheng Jin, and Jiaqi Wang. Unified reward model for multimodal understanding and generation. *arXiv preprint arXiv:2503.05236*, 2025.
- [39] Jacob Austin, Daniel D. Johnson, Jonathan Ho, Daniel Tarlow, and Rianne van den Berg. Structured denoising diffusion models in discrete state-spaces. In *Advances in Neural Information Processing Systems (NeurIPS)*, 2021.
- [40] Aaron Lou, Chenlin Meng, and Stefano Ermon. Discrete diffusion modeling by estimating the ratios of the data distribution. In *Proceedings of the International Conference on Machine Learning (ICML)*, 2024.
- [41] Shansan Gong, Shivam Agarwal, Yizhe Zhang, Jiacheng Ye, Lin Zheng, Mukai Li, Chenxin An, Peilin Zhao, Wei Bi, Jiawei Han, et al. Scaling diffusion language models via adaptation from autoregressive models. In *Proceedings of the International Conference on Learning Representations (ICLR)*, 2025.
- [42] Shen Nie, Fengqi Zhu, Zebin You, Xiaolu Zhang, Jingyang Ou, Jun Hu, Jun Zhou, Yankai Lin, Ji-Rong Wen, and Chongxuan Li. Large language diffusion models. *arXiv preprint arXiv:2502.09992*, 2025.
- [43] Fengqi Zhu, Rongzhen Wang, Shen Nie, Xiaolu Zhang, Chunwei Wu, Jun Hu, Jun Zhou, Jianfei Chen, Yankai Lin, Ji-Rong Wen, and Chongxuan Li. LLaDA 1.5: Variance-reduced preference optimization for large language diffusion models. *arXiv preprint arXiv:2505.19223*, 2025.
- [44] Zebin You, Shen Nie, Xiaolu Zhang, Jun Hu, Jun Zhou, Zhiwu Lu, Ji-Rong Wen, and Chongxuan Li. LLaDA-V: Large language diffusion models with visual instruction tuning. *arXiv preprint arXiv:2505.16933*, 2025.
- [45] Qingyu Shi, Jinbin Bai, Zhuoran Zhao, Wenhao Chai, Kaidong Yu, Jianzong Wu, Shuangyong Song, Yunhai Tong, Xiangtai Li, Xuelong Li, and Shuicheng Yan. Muddit: Liberating generation beyond text-to-image with a unified discrete diffusion model, 2025.
- [46] Ye Tian, Ling Yang, Jiongfeng Yang, Anran Wang, Yu Tian, Jiani Zheng, Haochen Wang, Zhiyang Teng, Zhuochen Wang, Yinjie Wang, Yunhai Tong, Mengdi Wang, and Xiangtai Li. Mmada-parallel: Multimodal large diffusion language models for thinking-aware editing and generation. *arXiv preprint arXiv:2511.09611*, 2025.
- [47] Yi Xin, Siqi Luo, Qi Qin, Haoxing Chen, Kaiwen Zhu, Zhiwei Zhang, Yangfan He, Rongchao Zhang, Jinbin Bai, Shuo Cao, et al. dmllm-tts: Self-verified and efficient test-time scaling for diffusion multi-modal large language models. *arXiv preprint arXiv:2512.19433*, 2025.
- [48] Kaiwen Zhu, Quansheng Zeng, Yuandong Pu, Shuo Cao, Xiaohui Li, Yi Xin, Qi Qin, Jiayang Li, Yu Qiao, Jinjin Gu, and Yihao Liu. Accelerating masked image generation by learning latent controlled dynamics. *arXiv preprint arXiv:2602.23996*, 2025.
- [49] Shengjun Zhang, Zhang Zhang, Chensheng Dai, and Yueqi Duan. E-GRPO: High entropy steps drive effective reinforcement learning for flow models. *arXiv preprint arXiv:2601.00423*, 2026.

Supplementary Material

A Related Work

A.1 Diffusion Multi-Modal Large Language Models

Discrete diffusion modeling is rapidly emerging as a highly promising paradigm, showing great potential to replace the traditional autoregressive (AR) modeling. Early discrete diffusion methods [39, 40] built the foundation for this shift by establishing the core principles of token-level denoising. Building on these methods, diffusion large language models (dLLMs) [41, 42, 43] show that text generation can be treated as a parallel and iterative denoising process. Expanding this framework to multi-modal domains, LLaDA-V [44] used visual instruction tuning to show that diffusion models can effectively combine visual and textual data. Driven by this progress, recent studies focus on developing unified diffusion multi-modal large language models (dMLLMs) [13, 45, 14, 16]. These models further extend the capabilities of image generation. This success also inspires new research on downstream applications for dMLLMs. Key areas include reinforcement learning algorithm design [19, 13], image editing [46], test-time scaling [47], and sampling acceleration [48].

A.2 Reinforcement Learning Alignment for dMLLMs

Applying Reinforcement Learning (RL) to discrete diffusion models introduces unique challenges, primarily because dynamic masking breaks the standard policy gradient assumption. To bypass this, existing works generally diverge into two directions. Random remasking methods [19, 20, 21] approximate intermediate states by randomly masking tokens. While maintaining the efficiency of a single forward pass, these approximated contexts often deviate from the actual denoising trajectory. Conversely, trajectory recording methods [22, 23, 24, 25] cache the entire denoising process to build a precise Markov Decision Process (MDP). However, this rigorosity comes at a heavy price, as the computational and memory costs scale linearly with the number of denoising steps. Crucially, both paradigms share a fundamental flaw: they uniformly assign the final reward to all tokens, ignoring prior insights [49] that early, high-entropy steps matter more for generation quality.

B A Unified Theoretical Framework for dMLLM RL Methods

This section formalizes the two existing approaches described in Section 2, random remasking methods and trajectory recording methods, together with HT-GRPO. We use g , i , k , and c for rollout index, token position, inner-loop update index, and text prompt condition respectively. All other symbols follow the notation in the main text.

As established in Section 2.3, the surrogate ideal objective \mathcal{J}^* (Eq. (4)) requires averaging over all valid denoising trajectories $\tau \in \mathcal{T}$, which is combinatorially intractable. All three paradigms therefore share the same clipped surrogate objective and differ only in three design choices: the conditioning context $\mathbf{C}_{g,i}^{(k)}$, the optimization support set $\mathcal{M}_g^{(k)}$, and the token-level weight $w_{g,i}$. Setting these to the choices in Section 3 recovers HT-GRPO exactly.

$$\mathcal{L}^{(k)}(\theta) = \frac{1}{G} \sum_{g=1}^G \frac{1}{|\mathcal{M}_g^{(k)}|} \sum_{i \in \mathcal{M}_g^{(k)}} \min\left(r_{g,i}^{(k)}(\theta) \tilde{A}_{g,i}, \text{clip}\left(r_{g,i}^{(k)}(\theta), 1 - \epsilon, 1 + \epsilon\right) \tilde{A}_{g,i}\right), \quad (12)$$

where

$$r_{g,i}^{(k)}(\theta) = \frac{\pi_{\theta}(v_{g,i} | \mathbf{C}_{g,i}^{(k)}, c)}{\pi_{\theta_{\text{old}}}(v_{g,i} | \mathbf{C}_{g,i}^{(k)}, c)}. \quad (13)$$

Here, $k \in \{1, \dots, K\}$ indexes the inner-loop gradient step, and the same rollout batch is reused for all K updates. $v_{g,i}$ is the token value generated at position i in rollout g . $\mathcal{M}_g^{(k)}$ is the optimization support set, the set of token positions that contribute gradients in the k -th inner-loop update. The conditioning context $\mathbf{C}_{g,i}^{(k)}$ is the partially observed token configuration used to evaluate the importance ratio for

position i in update k . The token-level weighted advantage $\tilde{A}_{g,i} = w_{g,i}A_g$ scales the group-relative advantage A_g by a per-token credit weight $w_{g,i}$, where

$$A_g = \frac{R_g - \text{mean}(\{R_j\})}{\text{std}(\{R_j\}) + \delta_m}. \quad (14)$$

The three methods differ only in how they instantiate these three quantities.

B.1 Random Remasking Methods

Random remasking methods, including MaskGRPO [19], D1 [20], and UniGRPO [21], retain only the final image \mathbf{x}_g and construct synthetic contexts by independently remasking each position with probability γ_k :

$$\begin{aligned} \mathcal{M}_g^{(k)} &= \{i : i \text{ is remasked with prob. } \gamma_k\} && \text{(support set),} \\ \mathbf{C}_{g,i}^{(k)} &= \text{Mask}(\mathbf{x}_g, \mathcal{M}_g^{(k)}) && \text{(mask } \mathcal{M}_g^{(k)}; \text{ retain token values elsewhere),} \\ w_{g,i} &= 1 && \text{(uniform weight).} \end{aligned} \quad (15)$$

Stage conflation. Because remasking is independent of the generation-order rank $\rho_{g,i}$, the support set $\mathcal{M}_g^{(k)}$ mixes structural tokens (small $\rho_{g,i}$) and refinement tokens (large $\rho_{g,i}$) in the same update with equal probability. By [Proposition C.1](#), these two groups carry fundamentally different levels of uncertainty, so their gradients operate at very different scales within a single update step.

Future-token contamination. The context $\mathbf{C}_{g,i}^{(k)}$ retains all positions not in $\mathcal{M}_g^{(k)}$. For position i , define the future token set as $\mathcal{F}_i^{(g)} = \{j : \rho_{g,j} > \rho_{g,i}\}$. Since remasking ignores generation order, each position in $\mathcal{F}_i^{(g)}$ is retained in $\mathbf{C}_{g,i}^{(k)}$ with probability $1 - \gamma_k$, potentially exposing tokens that had not yet been generated when position i was predicted. [Proposition C.2](#) shows this occurs with strictly positive probability for any non-final position.

Multi-path coverage (partial). Different random masks induce diverse conditioning contexts, exploring a broader range of token-context combinations than a single fixed trajectory. Random remasking is agnostic to generation order, however, so the resulting contexts are not guaranteed to correspond to any valid denoising trajectory. Because the context may include future tokens, as shown in the contamination analysis above, the diverse paths explored do not respect the causal ordering of the original generation process. The approximation of \mathcal{J}^* is therefore partial: broader in context diversity than a single trajectory, but biased away from the causal structure that \mathcal{J}^* requires.

Uniform token reward (unresolved). All positions receive the same credit weight $w_{g,i} = 1$ regardless of their generation-order rank. Structural and refinement tokens carry fundamentally different entropy levels and play different roles in image generation, as established in [Section 2.3](#). Equal credit assignment ignores this asymmetry entirely.

B.2 Trajectory Recording Methods

Trajectory recording methods, including TraceRL [22], CJ-GRPO [23], d-TreeRPO [24], and AGRPO [25], record the denoising order and evaluate each token under its trajectory-consistent conditioning context:

$$\begin{aligned} \mathcal{M}_g^{(k)} &= \{1, \dots, N\} && \text{(all } N \text{ tokens per update),} \\ \mathbf{C}_{g,i}^{(k)} &= \mathbf{x}_g^{(<i)} && \text{(reveals } \{j : \rho_{g,j} < \rho_{g,i}\}; \text{ remaining positions masked),} \\ w_{g,i} &= 1 && \text{(uniform weight).} \end{aligned} \quad (16)$$

Stage conflation (avoided). Unlike random remasking methods, which apply the same synthetic context to all tokens in $\mathcal{M}_g^{(k)}$ regardless of generation rank, trajectory recording methods set $\mathcal{M}_g^{(k)} = \{1, \dots, N\}$ and assign each token its own trajectory-consistent context $\mathbf{C}_{g,i}^{(k)} = \mathbf{x}_g^{(<i)}$. Structural tokens therefore receive sparse contexts reflecting their early generation stage, while refinement tokens receive progressively richer contexts. Each importance ratio is computed under a context that

matches the entropy level of the corresponding token, avoiding the uniform-context mismatch that characterizes stage conflation.

Future-token contamination (avoided). The trajectory-consistent context $\mathbf{C}_{g,i}^{(k)} = \mathbf{x}_g^{(<i)}$ reveals only positions with $\rho_{g,j} < \rho_{g,i}$. All positions in the future token set $\mathcal{F}_i^{(g)} = \{j : \rho_{g,j} > \rho_{g,i}\}$ are masked by construction, so future-token contamination cannot occur.

Limited path coverage. Both $\mathcal{M}_g^{(k)}$ and $\mathbf{C}_{g,i}^{(k)}$ are derived from a single rollout trajectory, so each update evaluates only one element of the expectation in Eq. (4). The many other valid trajectories $\tau \in \mathcal{T}$ that could produce the same image are never seen, restricting the diversity of generation paths the model learns from.

Uniform token reward (unresolved). All positions receive the same credit weight $w_{g,i} = 1$. Although the trajectory-consistent context $\mathbf{x}_g^{(<i)}$ naturally differentiates the conditioning richness of structural versus refinement tokens, the advantage broadcast to each token remains uniform. There is no explicit mechanism to amplify the learning signal for high-uncertainty structural tokens or attenuate it for near-deterministic refinement tokens.

B.3 HT-GRPO

HT-GRPO retains the final sample together with the generation-order rank $\rho_{g,i} \in \{1, \dots, N\}$, which records the unmasking step at which position i was revealed in rollout g , with $\rho_{g,i} = 1$ for the first token and $\rho_{g,i} = N$ for the last. Positions unmasked in the same denoising step share the same context and entropy level despite receiving different rank values. HT-GRPO partitions tokens into global, structural, and refinement groups:

$$\begin{aligned} \mathcal{S}_{g,\text{global}} &= \{1, \dots, N\}, \\ \mathcal{S}_{g,\text{structure}} &= \{i : \rho_{g,i} \leq N_s\}, \\ \mathcal{S}_{g,\text{refinement}} &= \{i : \rho_{g,i} > N_s\}, \end{aligned} \quad (17)$$

where $N_s = \lfloor \alpha N \rfloor$ and $K = n_{\text{global}} + n_{\text{structure}} + n_{\text{refinement}}$ is the total number of inner-loop updates. The K steps follow a fixed Global \rightarrow Structure \rightarrow Refinement schedule, and the support set at step k is a random subset drawn from the active stage:

$$\mathcal{M}_g^{(k)} \subseteq \begin{cases} \mathcal{S}_{g,\text{global}}, & 1 \leq k \leq n_{\text{global}}, \\ \mathcal{S}_{g,\text{structure}}, & n_{\text{global}} < k \leq n_{\text{global}} + n_{\text{structure}}, \\ \mathcal{S}_{g,\text{refinement}}, & n_{\text{global}} + n_{\text{structure}} < k \leq K. \end{cases} \quad (18)$$

All tokens share the same fully masked conditioning context, defined as the state in which all N image positions remain masked:

$$\mathbf{C}_{g,i}^{(k)} \equiv \mathbf{C}_\emptyset. \quad (19)$$

Token weights are generation-order-aware rather than uniform:

$$\begin{aligned} \tilde{A}_{g,i} &= w_{g,i} A_g, \\ w_{g,i} &= \begin{cases} \lambda_s, & i \in \mathcal{S}_{g,\text{structure}}, \\ \lambda_r, & i \in \mathcal{S}_{g,\text{refinement}}. \end{cases} \end{aligned} \quad (20)$$

Stage conflation (resolved). At each inner-loop step k , the support set $\mathcal{M}_g^{(k)}$ is drawn exclusively from the token set of the active stage. The Global \rightarrow Structure \rightarrow Refinement schedule partitions the K updates by generation rank, so high-entropy structural tokens and low-entropy refinement tokens are never placed in the same $\mathcal{M}_g^{(k)}$. The entropy gap between these two groups is established in [Proposition C.1](#). This resolves the stage conflation identified in [Section 2.3](#).

Future-token contamination (eliminated). Setting $\mathbf{C}_{g,i}^{(k)} \equiv \mathbf{C}_\emptyset$ masks all N positions uniformly for every token and every update, making future-token exposure impossible by construction. Contamination is eliminated without requiring trajectory storage, as formalized in [Proposition C.2](#).

Limited path coverage (alleviated). Within each stage, $\mathcal{M}_g^{(k)}$ is re-sampled independently at every inner-loop step according to an annealed sampling rate $\gamma_{k_s}^{(s)}$ ([Appendix F.1](#)). Different token subsets

receive gradient signal across the K updates, providing Monte Carlo coverage of the token space within each stage and partially alleviating the single-trajectory limitation. Because \mathbf{C}_\emptyset decouples the importance ratio from any particular ordering, this intra-stage sampling introduces no causal inconsistency.

Uniform token reward (resolved). The per-token weight $w_{g,i}$ assigns $\lambda_s > 1$ to structural tokens and $\lambda_r < 1$ to refinement tokens, replacing the uniform $w_{g,i} = 1$ used by both existing families. This amplifies gradient updates on global composition and attenuates updates on near-deterministic local detail, following the rationale in Section 3.2. Trajectory recording methods avoid stage conflation and future-token contamination but leave credit assignment uniform. HT-GRPO is therefore the only paradigm that addresses all four limitations.

B.4 Comparison

Table 4 summarizes the three paradigms along eight dimensions. The formal basis for the entropy-related entries is provided in Section C (Propositions C.1–C.3). Among the four limitations identified in Section 2.3, random remasking methods introduce stage conflation and future-token contamination while achieving only partial path coverage. Trajectory recording methods avoid the first two but sacrifice path diversity and require $O(T)$ forward passes per rollout. Neither family addresses the uniform token reward problem. HT-GRPO resolves all four: inter-stage partitioning eliminates stage conflation, \mathbf{C}_\emptyset eliminates future-token contamination, intra-stage random subsets partially alleviate limited path coverage, and generation-order-aware weights $w_{g,i}$ replace uniform credit assignment.

Table 4: Comparison of three dMLLM RL paradigms under a unified formulation. Limitation rows correspond to the four issues identified in Section 2.3.

Dimension	Random Remasking	Trajectory Recording	HT-GRPO
<i>Design choices</i>			
Support set $\mathcal{M}_g^{(k)}$	Remasked positions	All N tokens	Random subset of active stage
Conditioning context $\mathbf{C}_{g,i}^{(k)}$	Randomly retained tokens after remasking	True rollout state $\mathbf{x}_g^{(<i)}$	Fully masked state \mathbf{C}_\emptyset
Token weight $w_{g,i}$	Uniform (= 1)	Uniform (= 1)	Generation-order-aware ($\lambda_s > 1, \lambda_r < 1$)
<i>Operational cost</i>			
Trajectory storage	Final image only	All T intermediate states	Generation-order ranks $\rho_{g,i}$
Forward passes per inner loop	1	T	1
<i>Limitation analysis</i>			
Stage conflation	Yes	No	Resolved
Future-token contamination	Yes	No	Eliminated
Multi-path coverage	Partial (causally inconsistent)	Limited (single trajectory)	Alleviated (intra-stage sampling)
Uniform token reward	Unresolved	Unresolved	Resolved

C Information-Theoretic Basis of Hierarchical Token Grouping and the Prompt-Conditioned Estimator

We establish three formal results underpinning HT-GRPO’s design.

Assumption (Approximate Consistency). Let V_i be the token at position i , p_θ the joint generation distribution, and $\mathbf{C}^{[n]}$ any partially revealed context with n positions unmasked and position i still masked. We assume the model’s prediction matches the true conditional:

$$\pi_\theta(\cdot \mid \mathbf{C}^{[n]}, c) = p_\theta(\cdot \mid \mathbf{C}^{[n]}, c). \quad (21)$$

This connects the model’s output to standard information-theoretic quantities. We write $H(\pi_\theta(\cdot | \mathbf{C}, c))$ for the **predictive entropy**, which measures how uncertain the model is about position i given visible context \mathbf{C} . **Propositions C.1** and **C.3** additionally require that $\mathbf{C}^{[n']}$, where $n' > n$, is obtained from $\mathbf{C}^{[n]}$ by revealing more tokens along the same trajectory while keeping position i masked.

Proposition C.1 (Entropy Monotonicity). *Seeing more context reduces uncertainty.* Under Assumption (21), for any position i and any $0 \leq n < n' \leq N-1$,

$$\mathbb{E}_{\mathbf{C}^{[n]}} \left[H \left(\pi_\theta(\cdot | \mathbf{C}^{[n]}, c) \right) \right] \geq \mathbb{E}_{\mathbf{C}^{[n']}} \left[H \left(\pi_\theta(\cdot | \mathbf{C}^{[n']}, c) \right) \right]. \quad (22)$$

Proof. Let \mathbf{D} be the additional tokens revealed between $\mathbf{C}^{[n]}$ and $\mathbf{C}^{[n']}$. Since mutual information is non-negative, $I(V_i; \mathbf{D} | \mathbf{C}^{[n]}, c) = H(V_i | \mathbf{C}^{[n]}, c) - H(V_i | \mathbf{C}^{[n']}, c) \geq 0$. Applying Assumption (21) to both sides yields the stated inequality. \square

Tokens unmasked early (small $\rho_{g,i}$, few context tokens visible) therefore carry higher uncertainty than those unmasked late. Tokens sharing the same denoising step share the same context and entropy level despite having different $\rho_{g,i}$ values. This justifies treating early tokens as structural tokens and late tokens as refinement tokens ($\mathcal{S}_{g,\text{structure}}$, $\mathcal{S}_{g,\text{refinement}}$ in Section 3.1).

Definition (Future-token set). For rollout g and position i , define $\mathcal{F}_i^{(g)} = \{j : \rho_{g,j} > \rho_{g,i}\}$ as the set of tokens unmasked *after* i . These tokens are still masked when i is predicted; if any appear in the conditioning context, they inject future information into the current optimization step.

Proposition C.2 (Future-Token Contamination). *Random remasking exposes future tokens with nonzero probability, misspecifying the conditioning distribution.* In random remasking methods, each position is independently remasked with probability $p_k \in (0, 1)$. For any non-final position i , at least one future token from $\mathcal{F}_i^{(g)}$ remains visible in $\mathbf{C}_{g,i}^{(k)}$ with probability

$$\Pr[\mathbf{C}_{g,i}^{(k)} \not\equiv \mathbf{x}_g^{(<i)}] = 1 - p_k^{|\mathcal{F}_i^{(g)}|} > 0. \quad (23)$$

In the true trajectory context $\mathbf{x}_g^{(<i)}$ all future positions are masked; when contamination occurs, the ratio $\tilde{r}_{g,i}(\theta) = \pi_\theta(v_{g,i} | \mathbf{C}_{g,i}^{(k)}, c) / \pi_{\theta_{\text{old}}}(v_{g,i} | \mathbf{C}_{g,i}^{(k)}, c)$ is evaluated under a causally inconsistent context, leading to a misspecified policy gradient estimator.

Proof. The $|\mathcal{F}_i^{(g)}|$ future positions are remasked independently; all are correctly masked with probability $p_k^{|\mathcal{F}_i^{(g)}|}$, so the complement gives the contamination probability. In $\mathbf{x}_g^{(<i)}$, all future positions are masked by definition, confirming the context mismatch. \square

Thus, random remasking methods evaluate the likelihood ratio under a conditioning distribution that differs from the trajectory-consistent one.

Remark. Let $r_{g,i}^*(\theta) = \pi_\theta(v_{g,i} | \mathbf{x}_g^{(<i)}, c) / \pi_{\theta_{\text{old}}}(v_{g,i} | \mathbf{x}_g^{(<i)}, c)$ denote the trajectory-consistent ratio, where $\mathbf{x}_g^{(<i)}$ is the true denoising state just before token i is revealed (Section B). The claim above concerns the *conditioning distribution*, not a guaranteed pointwise inequality: $\tilde{r}_{g,i}$ and $r_{g,i}^*$ could coincide numerically for specific θ , but whenever contamination occurs the estimator is structurally inconsistent with the trajectory-consistent objective.

Unlike $\mathbf{x}_g^{(<i)}$, \mathbf{C}_\emptyset additionally masks past tokens, so HT-GRPO does not recover $r_{g,i}^*$. This is a deliberate design choice: exact computation of $r_{g,i}^*$ requires marginalizing over all mask configurations consistent with the generation order, which is combinatorially intractable (Section 3). HT-GRPO instead defines a *unified* estimator using the same context \mathbf{C}_\emptyset for every token:

$$\hat{r}_{g,i}(\theta) = \frac{\pi_\theta(v_{g,i} | \mathbf{C}_\emptyset, c)}{\pi_{\theta_{\text{old}}}(v_{g,i} | \mathbf{C}_\emptyset, c)}. \quad (24)$$

This estimator has three properties. First, it is contamination-free by construction. Second, it is self-consistent: the conditioning context is identical for both policies, ensuring a well-defined likelihood ratio. Third, it is entropy-preserving: predictive entropy under \mathbf{C}_\emptyset is not smaller in expectation than under contexts that condition on additional structural token information (**Proposition C.3**), which maintains reward variance and prevents GRPO advantage collapse.

Table 5: **Ablation study on random-subset annealing.** All experiments use $\alpha = 0.3$ and $n_g : n_s : n_r = 2 : 4 : 2$.

Coverage strategy	$(\gamma_{\max}, \gamma_{\min}, \phi)$	Single	Two Obj.	Count	Color	Pos.	Attr.	Overall
Full coverage	(1.0, 1.0, constant)	100.00	87.88	72.50	92.55	64.00	62.00	79.82
Fixed sparse sampling	(0.2, 0.2, constant)	97.50	85.86	75.00	87.23	70.00	67.00	80.43
Ascending annealing	(1.0, 0.5, up)	100.00	91.92	76.25	88.30	72.00	66.00	82.41
Linear decay (ours)	(1.0, 0.5, down)	100.00	92.93	77.50	90.43	73.00	66.00	83.31

Proposition C.3 (Entropy Lower Bound under Full Masking). *Revealing structural tokens reduces uncertainty over refinement tokens.* Let $\mathbf{S} = \{V_j : j \in \mathcal{S}_{g,\text{structure}}\}$ denote the structural token values and $\mathbf{x}^{\text{structure}}(\mathbf{S})$ the context revealing only those positions. For any refinement token $i \notin \mathcal{S}_{g,\text{structure}}$,

$$H(\pi_\theta(\cdot \mid \mathbf{C}_\emptyset, c)) \geq \mathbb{E}_{\mathbf{S}} [H(\pi_\theta(\cdot \mid \mathbf{x}^{\text{structure}}(\mathbf{S}), c))]. \quad (25)$$

Proof. By Assumption (21), the left side equals $H(V_i \mid c)$ and the right side equals $H(V_i \mid \mathbf{S}, c)$. Non-negativity of $I(V_i; \mathbf{S} \mid c) = H(V_i \mid c) - H(V_i \mid \mathbf{S}, c) \geq 0$ gives the result. \square

In practice, once structural layout is fixed, refinement tokens become nearly deterministic: most rollouts look alike, reward variance collapses, and the GRPO advantage shrinks toward zero. This is **conditional low-entropy degradation** (Section 3). Using \mathbf{C}_\emptyset avoids revealing any structural layout, keeping entropy high and preserving the learning signal.

D Standard GRPO Objective

Given a prompt q , GRPO [26] samples G complete outputs $\{o_i\}_{i=1}^G$ from the behavior policy $\pi_{\theta_{\text{old}}}$ and maximizes the clipped surrogate objective:

$$\mathcal{J}_{\text{GRPO}}(\theta) = \mathbb{E}_{q, \{o_i\} \sim \pi_{\theta_{\text{old}}}} \left[\frac{1}{G} \sum_{i=1}^G \frac{1}{|o_i|} \sum_{t=1}^{|o_i|} \min(r_{i,t}(\theta) \hat{A}_i, \text{clip}(r_{i,t}(\theta), 1-\epsilon, 1+\epsilon) \hat{A}_i) - \beta \mathbb{D}_{\text{KL}}(\pi_\theta \parallel \pi_{\text{ref}}) \right], \quad (26)$$

where the importance ratio

$$r_{i,t}(\theta) = \frac{\pi_\theta(o_{i,t} \mid q, o_{i,<t})}{\pi_{\theta_{\text{old}}}(o_{i,t} \mid q, o_{i,<t})} \quad (27)$$

measures the relative likelihood of token $o_{i,t}$ under the current policy versus the behavior policy, given the same causal prefix $o_{i,<t}$. The group-relative advantage

$$\hat{A}_i = \frac{R_i - \text{mean}(\{R_j\}_{j=1}^G)}{\text{std}(\{R_j\}_{j=1}^G) + \delta} \quad (28)$$

is a scalar derived from the outcome reward R_i and broadcast uniformly to all tokens in output o_i . In practice, the same sampled batch $\{o_i\}$ is reused for K successive gradient steps, with all importance ratios computed relative to the fixed behavior policy $\pi_{\theta_{\text{old}}}$.

E Ablation Study Details

All ablations run on MMaDA with $K = 8$ and $\alpha = 0.3$ unless otherwise stated.

A1: Staged RL Training is Necessary for dMLLMs. Figure 4(a) compares various budget allocation strategies under a fixed inner-loop budget $K = 8$. Both single-stage and two-stage variants yield limited overall performance, scoring only between 78.3 and 80.2. The full three-stage Sketch-Then-Paint schedule (Global \rightarrow Structure \rightarrow Refinement with a 2:4:2 budget) breaks this bottleneck, reaching 83.3 overall, confirming that the coarse-to-fine ordering itself—not merely token-group separation—drives the gain.

During the twilight hour, an individual can be seen extending an arm towards the sky, pointing at a **trio of wild birds** gliding through the rich deep blue of the early evening sky. The birds' silhouettes contrast distinctly against the fading light, their wings spread wide as they soar. The person is silhouetted against the dusky sky, creating a peaceful scene of human connection with nature.



On a rustic wooden table, **three ripe eggplants** with a glossy royal purple skin are carefully arranged in a neat row. Their plump, oblong shapes complement the table's textured surface, and they cast soft shadows in the warm, ambient light. Nearby, the woven pattern of a tan-colored napkin peeks out from beneath the vibrant, richly colored vegetables.

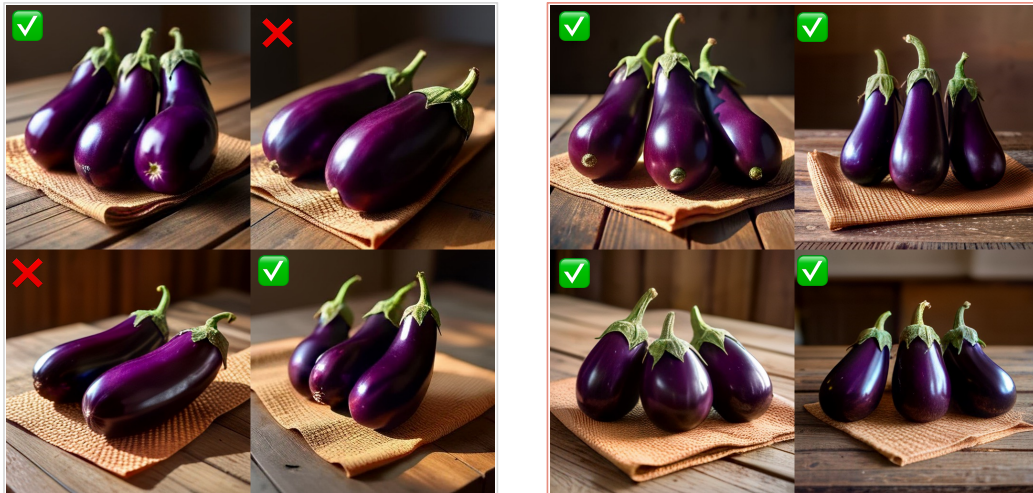
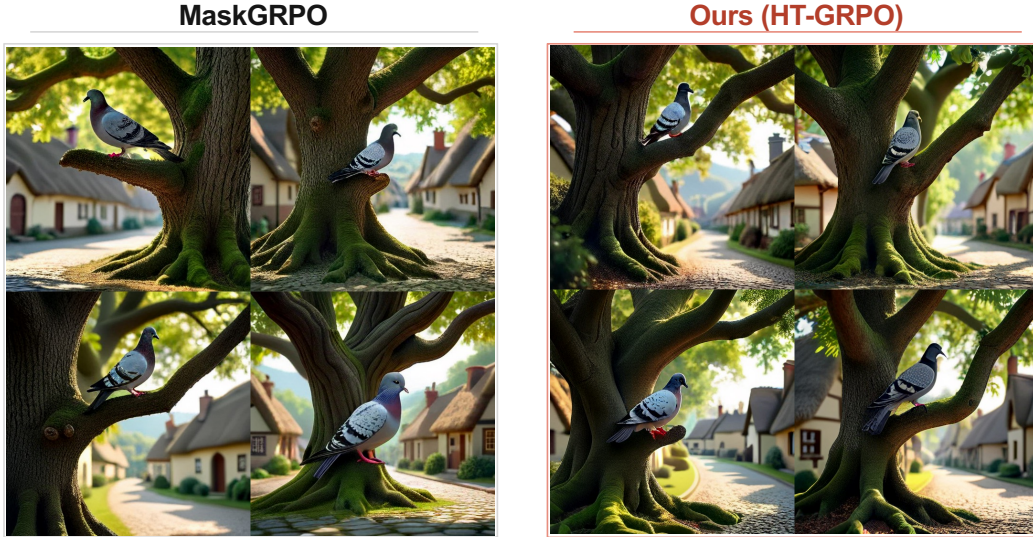


Figure 5: **DPG-Bench counting examples on Lumina-DiMOO.** For each prompt, we compare four samples per method: MaskGRPO on the left and HT-GRPO on the right. HT-GRPO more consistently preserves the requested object count.

A2: Structure-biased Budget Allocation Maximizes Returns. Figure 4(a) also explores budget distribution across stages. The default 2:4:2 allocation achieves the best overall score of 83.3. Refinement-biased (2:2:4) and global-biased (4:2:2) allocations underperform, indicating that structural tokens require more optimization steps to resolve layout and compositional relations.

A3: Superiority of Coarse-to-fine Annealing Schedule. Table 5 evaluates how the annealing schedule controls token sampling within each stage. Static strategies—constant full coverage ($\gamma_{\max}=\gamma_{\min}=1.0$, 79.82) and fixed sparse sampling ($\gamma_{\max}=\gamma_{\min}=0.2$, 80.43)—both underperform

A robust pigeon, with grey and white feathered plumage, sits comfortably on the sturdy branch of a venerable oak tree, replete with sprawling arms and knotted bark. Below, the mossy roots of the tree stretch out into the cobblestone paths of a charming village, where small, thatched-roof cottages neighbor each other. Sunlight dapples through the dense leaf canopy above, casting playful shadows on the scene below.



A majestic parrot with vibrant green, red, and blue feathers glides effortlessly across the bright blue sky. Its impressive wingspan is fully outstretched, catching the warm sunlight as it soars high above the tree line. Below, the landscape features rolling hills and patches of dense forest.



Figure 6: **DPG-Bench scene-level structural completeness on Lumina-DiMOO.** Each prompt compares MaskGRPO and HT-GRPO with four samples per method. HT-GRPO better preserves relative scale, foreground-background structure, and subject pose across complex scene descriptions.

dynamic variants. Ascending annealing ($\gamma: 0.5 \rightarrow 1.0$, 82.41) improves over static baselines but lags behind our method: starting with sparse coverage causes unstable gradient directions in early updates. Our linear decay schedule ($\gamma: 1.0 \rightarrow 0.5$) achieves the best overall score of **83.31**.

A4: Sensitivity to Structure Ratio α . Figure 4(b) evaluates the structural-group boundary. Performance peaks at $\alpha = 0.3$ (83.3). A smaller ratio ($\alpha = 0.1$) leaves many layout-relevant tokens under-optimized (80.2), while a larger ratio ($\alpha = 0.5$) dilutes the hierarchy by including tokens with rich visual context, both degrading performance.

A5: Ablation on Credit Weighting & Ratio Conditioning. Figure 4(c) examines the two components of Section 3.2 and Section 3.1.2. Discarding credit weights ($\lambda_s = \lambda_r = 1$) drops the overall score to 80.8, confirming that amplifying structural-token updates is critical for layout composition. Replacing C_\emptyset with revealed structural contexts yields 80.6: once the structural layout is exposed, refinement-token distributions become overly sharp, collapsing ratio variation and weakening the RL signal—precisely the conditional low-entropy degradation identified in Proposition C.3.

Table 6: **Hyperparameter settings used in all experiments.**

Category	Hyperparameter	Value
HT-GRPO	Structure ratio α	0.3
	Stage budget $n_{\text{global}} : n_{\text{structure}} : n_{\text{refinement}}$	2 : 4 : 2
	Structural weight λ_s	1.5
	Refinement weight λ_r	0.5
Annealing	Schedule mode ϕ	down
	γ_{max} (all stages)	1.0
	γ_{min} (all stages)	0.5
RL training	Rollouts per prompt G	9
	Classifier-free guidance scale	3.5
	Reward	HPSv3 + CLIP (ViT-L/14) + UniRwd
Hardware	GPUs	8 × A100-80G

F Implementation Supplement

F.1 Random-Subset Scheduling Functions

Let $k_s \in \{0, \dots, n_s - 1\}$ denote the within-stage update counter for stage s . The general sampling rate is

$$\gamma_{k_s}^{(s)} = \gamma_{\text{min}}^{(s)} + (\gamma_{\text{max}}^{(s)} - \gamma_{\text{min}}^{(s)}) \cdot \phi\left(\frac{k_s}{\max(1, n_s - 1)}\right), \quad (29)$$

where $\phi : [0, 1] \rightarrow [0, 1]$ is a shape function. The main text uses $\phi(p) = 1 - p$ (down mode), which specializes to Eq. (8):

$$\gamma_{k_s}^{(s)} = \gamma_{\text{min}}^{(s)} + (\gamma_{\text{max}}^{(s)} - \gamma_{\text{min}}^{(s)}) \cdot \frac{\max(1, n_s - 1) - k_s}{\max(1, n_s - 1)}. \quad (30)$$

We additionally support the following variants (Table 7):

Table 7: **Scheduling functions for random-subset annealing.**

Mode	$\phi(p)$	Behavior
down	$1 - p$	Linear decay from high coverage to low coverage
up	p	Linear growth from low coverage to high coverage
constant	$\frac{1}{2}$	Fixed coverage independent of progress

Each stage maintains its own $\gamma_{\text{max}}^{(s)}$ and $\gamma_{\text{min}}^{(s)}$, allowing different coverage ranges for the global, structural, and refinement stages.

F.2 Hyperparameter Settings

Table 6 lists all hyperparameters used in our experiments. HT-GRPO is implemented on top of the MaskGRPO codebase, inheriting its optimizer, KL penalty coefficient, and RL loop without modification; only the HT-GRPO-specific settings below are new.

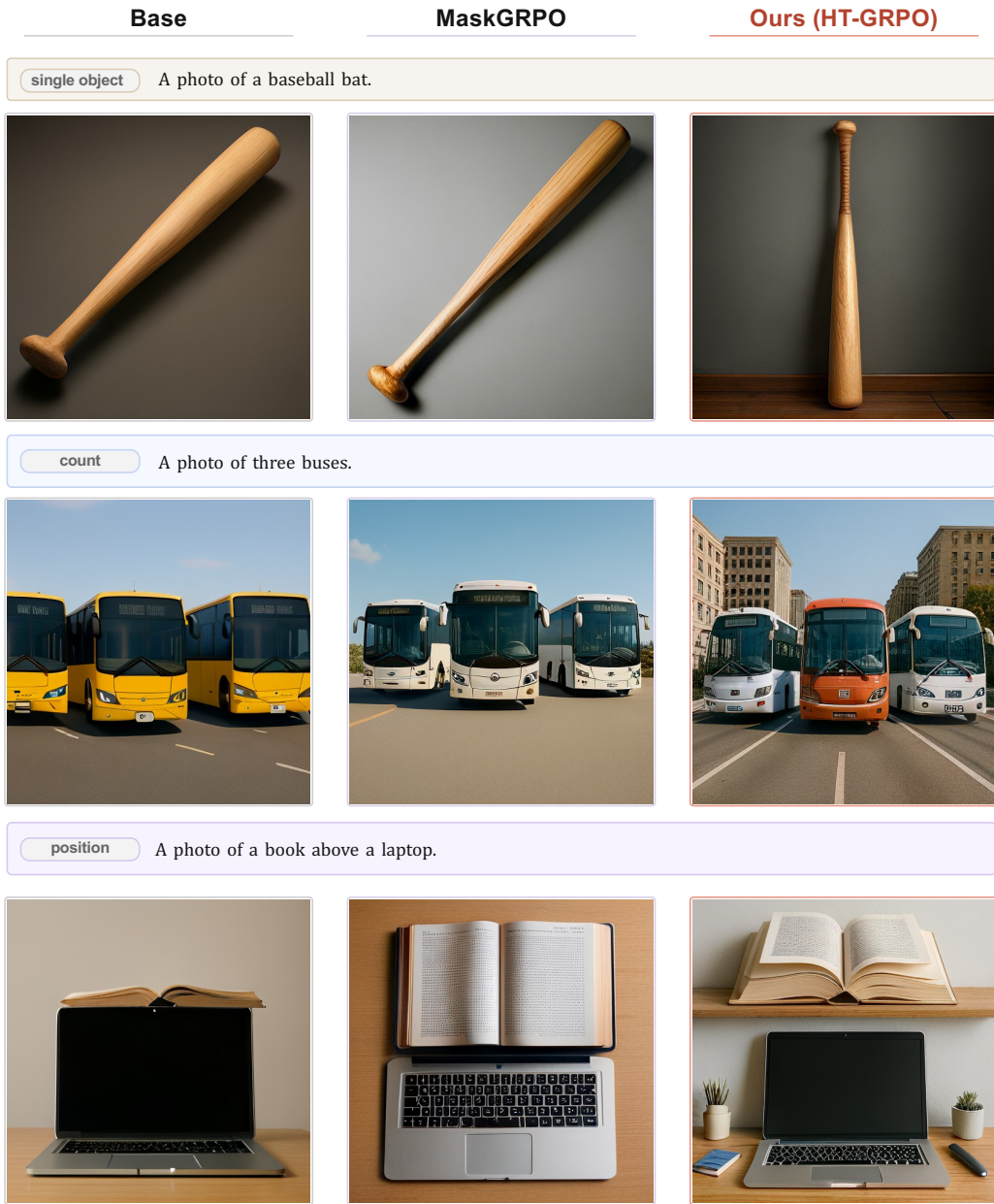


Figure 7: **GenEval qualitative comparison.** From left to right: base model, MaskGRPO, and HT-GRPO. HT-GRPO improves visual fidelity, object counting, and spatial relation grounding while producing more natural scene compositions.

G Qualitative Results

G.1 DPG-Bench: Counting Accuracy

Figure 5 compares MaskGRPO and HT-GRPO on two DPG-Bench prompts that require reliable counting on Lumina-DiMOO. The first prompt requires a person pointing toward a trio of birds, where the model must preserve both the object count and the human-object spatial relation. The second prompt requires exactly three eggplants arranged on a table. MaskGRPO often produces an incorrect number of target objects, while HT-GRPO more consistently satisfies the requested count.

Algorithm 1 HT-GRPO Training

Require: Policy π_θ , reference policy π_{ref} , reward function $R(\cdot)$, prompts $\{c\}$
Require: Structure fraction α , stage budgets $n_{\text{global}}, n_{\text{structure}}, n_{\text{refinement}}$
Require: Annealing rates $\gamma_{\text{max}}^{(s)}, \gamma_{\text{min}}^{(s)}$, credit weights λ_s, λ_r , clip ratio ϵ , KL coefficient β , stability constant δ

- 1: **for** each training iteration **do**
- 2: $\theta_{\text{old}} \leftarrow \theta$
 // Phase 1: Rollout
- 3: **for** $g = 1, \dots, G$ **do**
- 4: Sample $\mathbf{x}_g^{(0)}$ from $\pi_{\theta_{\text{old}}}$; record unmasking rank $\rho_{g,i}$ for each token i
- 5: Compute reward $R_g \leftarrow R(\mathbf{x}_g^{(0)}, c)$
- 6: **end for**
 // Phase 2: Token Partitioning
- 7: $N_s \leftarrow \lfloor \alpha N \rfloor$
- 8: $\mathcal{S}_{g,\text{structure}} \leftarrow \{i \mid \rho_{g,i} \leq N_s\}, \mathcal{S}_{g,\text{refinement}} \leftarrow \{i \mid \rho_{g,i} > N_s\}, \mathcal{S}_{g,\text{global}} \leftarrow \{1, \dots, N\}$
 // Phase 3: Reward & Hierarchical Credit Assignment
- 9: $A_g \leftarrow (R_g - \text{mean}(\{R_j\})) / (\text{std}(\{R_j\}) + \delta)$
- 10: $\tilde{A}_{g,i} \leftarrow \begin{cases} A_g \cdot \lambda_s & i \in \mathcal{S}_{g,\text{structure}} \\ A_g \cdot \lambda_r & i \in \mathcal{S}_{g,\text{refinement}} \end{cases}$
 // Phase 4: Sketch-Then-Paint Staged Optimization
- 11: **for** $s \in [\text{Global}, \text{Structure}, \text{Refinement}]$ **do**
- 12: **for** $k_s = 0, \dots, n_s - 1$ **do**
- 13: $\gamma_{k_s}^{(s)} \leftarrow \gamma_{\text{min}}^{(s)} + (\gamma_{\text{max}}^{(s)} - \gamma_{\text{min}}^{(s)}) \cdot \frac{\max(1, n_s - 1) - k_s}{\max(1, n_s - 1)}$
- 14: **for** $g = 1, \dots, G$ **do**
- 15: Sample $\mathcal{M}_g^{(k_s)} \subseteq \mathcal{S}_{g,s}$ with rate $\gamma_{k_s}^{(s)}$
- 16: **end for**
- 17: Compute $\pi_\theta(v_{g,i} \mid \mathbf{C}_\emptyset, c)$ for all $i \in \bigcup_g \mathcal{M}_g^{(k_s)}$ \triangleright single forward pass
- 18: $r_{g,i}(\theta) \leftarrow \pi_\theta(v_{g,i} \mid \mathbf{C}_\emptyset, c) / \pi_{\theta_{\text{old}}}(v_{g,i} \mid \mathbf{C}_\emptyset, c)$
- 19: $\mathcal{J}^{(k_s)} \leftarrow \frac{1}{G} \sum_{g=1}^G \frac{1}{|\mathcal{M}_g^{(k_s)}|} \sum_{i \in \mathcal{M}_g^{(k_s)}} \min(r_{g,i} \tilde{A}_{g,i}, \text{clip}(r_{g,i}, 1-\epsilon, 1+\epsilon) \tilde{A}_{g,i}) - \beta \mathbb{D}_{\text{KL}}(\pi_\theta \parallel \pi_{\text{ref}})$
- 20: $\theta \leftarrow \theta + \eta \nabla_\theta \mathcal{J}^{(k_s)}$
- 21: **end for**
- 22: **end for**
- 23: **end for**

This illustrates two benefits of the Sketch-Then-Paint hierarchy. First, counting is treated as a structural decision rather than a refinement detail. HT-GRPO updates all tokens in the Global stage and then focuses on structural tokens in the Structure stage, allowing the model to determine how many objects should appear and where they should be placed before local appearance is refined. Second, the staged inner loop prevents counting-related structural decisions from being diluted by refinement updates. MaskGRPO can mix structure and texture tokens in the same update, so the learning signal for object count and spatial placement competes with color and surface-detail optimization. HT-GRPO separates these roles by optimizing structure before refinement, making the correct count and layout more stable across samples.

G.2 DPG-Bench: Scene-Level Structural Completeness

Figure 6 compares MaskGRPO and HT-GRPO on two DPG-Bench prompts that require coherent scene-level structure and foreground-background composition. For the first prompt, both methods can generate the pigeon, oak tree, and village background, but MaskGRPO shows weaker spatial grounding: the tree roots are not always naturally connected to the ground, and the foreground tree can appear flattened against the village backdrop. The pigeon is also sometimes disproportionately

large relative to the tree and cottages, further weakening the scene hierarchy. HT-GRPO better preserves the spatial relationship among the pigeon, oak branches, tree trunk, roots, and village background, producing a more coherent foreground–background structure.

For the second prompt, which requires a parrot with fully outstretched wings flying above hills and forest, MaskGRPO can generate the target bird but often renders it with a flatter, less three-dimensional foreground structure. Its wing geometry and flying pose are less naturally integrated with the landscape. HT-GRPO more reliably preserves the outstretched wing structure, flying pose, and background scene context, resulting in a stronger sense of depth and scene-level coherence. These examples suggest that the Sketch-Then-Paint hierarchy helps establish global scene layout and object configuration before local appearance refinement.

G.3 GenEval: Spatial Grounding and Visual Fidelity

Figure 7 compares the base model, MaskGRPO, and HT-GRPO on representative GenEval examples covering single-object generation, object counting, and spatial relation understanding. Beyond improving correctness, HT-GRPO also produces more natural and visually diverse images. In the single-object example, all methods generate a baseball bat, while HT-GRPO renders a cleaner object with a more realistic scene composition. In the counting example, HT-GRPO preserves the requested three buses while producing a more diverse urban scene. The spatial-relation example is particularly illustrative: MaskGRPO tends to entangle the book and laptop into a single top-down composition, making the “book above laptop” relation ambiguous. In contrast, HT-GRPO separates the two objects into a clear vertical arrangement, placing the book above the laptop and enriching the scene with natural contextual elements. This suggests that HT-GRPO improves not only object-level accuracy, but also spatial grounding and aesthetic scene construction.

H Complete Training Algorithm

We propose HT-GRPO Training in Algorithm 1. For completeness, the entire training pipeline is summarized in a step-by-step form.